

# Efficient Charge Extraction out of Nanoscale Schottky Contacts to CdS Nanowires

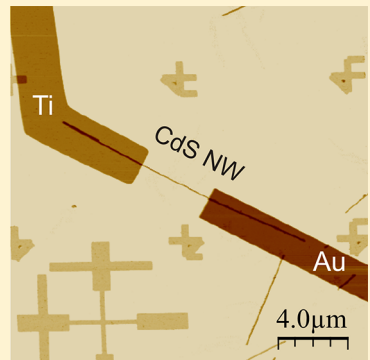
Thomas Dufaux,<sup>1,\*</sup> Marko Burghard,<sup>1</sup> and Klaus Kern<sup>1,2</sup>

<sup>1</sup>Max-Planck-Institut für Festkörperforschung, Heisenbergstrasse 1, 70569 Stuttgart, Germany

<sup>2</sup>Institute de Physique de la Matière Condensée, École Polytechnique Fédérale de Lausanne, 1015 Lausanne, Switzerland

## S Supporting Information

**ABSTRACT:** Charge recombination dynamics in semiconductor nanostructures is of vital importance for photovoltaic or photodetector device applications. We use local photocurrent measurements to explore spatially separated drift- and diffusion-currents close to the edge of gold contacts on top of cadmium sulfide nanowires. By theoretical modeling of the experimental photocurrent profiles, the electron diffusion length and lifetime in the wires are obtained to 0.8  $\mu\text{m}$  and 1 ns, respectively. In contrast to bulk devices, the nanoscale dimensions of the involved Schottky contacts enable a highly efficient charge carrier extraction from below the electrodes. This finding paves the way for designing nanostructured optoelectronic devices of improved performance.



**KEYWORDS:** Cadmium sulfide, nanowire, scanning photocurrent microscopy, recombination, Schottky contact

Semiconductor nanowires (NWs) are versatile components of optoelectronic devices, like solar cells<sup>1</sup> and photodetectors.<sup>2</sup> Owing to their high density of surface states, such wires can have a higher sensitivity to light than the corresponding bulk material.<sup>3–5</sup> Upon arranging the NWs into vertical arrays, the optical absorption can be further enhanced due to more efficient scattering.<sup>6,7</sup> Apart from the intrinsic material properties, the device performance depends sensitively on the electrical contacts.<sup>8</sup> Photodetectors often incorporate Schottky-type contacts because of their fast response time of 10 ps, which originates from the strong built-in electric fields, especially under reverse bias conditions.<sup>8</sup> A valuable tool to study such fields in nanoscale devices is provided by scanning photocurrent microscopy (SPCM).<sup>10</sup> This technique has been employed to study the photoelectric properties of materials, like CdS<sup>11</sup> or Si,<sup>12</sup> to determine electric potential steps at contacts,<sup>13</sup> to characterize electrostatic gating in graphene<sup>14</sup> as well as to explore plasmonic coupling at nanoscale contacts.<sup>15</sup>

In the present work, we evaluate the photocurrent response at the Schottky contact formed between a gold layer and a cadmium sulfide (CdS) NW. In this manner, diffusion currents can be effectively separated from the drift contribution, thus enabling reliable measurement of the electron diffusion length in the wires. This in turn yields the electron recombination rate at the metal contact, a quantity which otherwise is only indirectly accessible, for example, from the ideality factor of diode-type  $I/V$  curves.<sup>16</sup> The possibility to measure the charge recombination at a contact and to significantly reduce it by an appropriate contact design could promote the development of

novel, more efficient NW-based solar cells (including thin film devices) or photodetectors.

The CdS NWs were synthesized by a solvothermal process using an established protocol.<sup>8</sup> In order to obtain stable and reproducible photocurrent responses in the contact regions, it proved essential to remove the oxide from the NW surface. This was achieved by dispersing the wires in an aqueous HCl solution (pH 2) for 15 min at room temperature. Subsequently, the wire surface was passivated by attachment of an organic thiol layer (immersion in a 70  $\mu\text{L}/\text{mL}$  solution in ethanol for 48 h under ambient conditions, followed by three washing steps using pure ethanol). While we did not systematically study the suitability of different types of thiols, we obtained reproducible results with heptadecafluoro-1-decanethiol (Sigma-Aldrich) as ligand. All samples described in the following comprised CdS NWs capped with this thiol. The surface-functionalized NWs were deposited by spin coating (20  $\mu\text{L}$  droplet at 5000 rpm) from dispersion in ethanol onto a highly doped silicon substrate covered with a 300 nm thick layer of thermal SiO<sub>2</sub>. Subsequently, individual NWs were provided first with a gold contact extending over several micrometers on top of the wire. For this purpose, e-beam lithography was used followed by thermal evaporation of 80 nm of gold. The sample was then annealed at 350 °C for 15 min in argon atmosphere to improve the contact. Due to the high work function of the gold, a Schottky-like contact is formed at this electrode.<sup>17</sup> Finally, a

**Received:** November 29, 2011

**Revised:** May 7, 2012

**Published:** May 9, 2012

second contact made of titanium was defined at a separation of  $\sim 5 \mu\text{m}$  from the edge of the gold contact. Before evaporation of 80 nm titanium, the sample was subjected to argon plasma ( $P = 200 \text{ W}$ ,  $p = 0.3 \text{ Torr}$ ,  $t = 2 \text{ min}$ ) in order to locally n-dope the contact area<sup>18</sup> and thereby ensure an ohmic contact.<sup>11</sup> The SPCM studies were performed under ambient conditions using a laser wavelength of 488 nm, a  $50\times$  objective (NA = 0.8), and a light intensity of  $\sim 190 \text{ kW/cm}^2$ . The device behavior presented below has been reproducibly observed on four devices.

Figure 1a shows an AFM image of a completed CdS NW device. The combination of an ohmic and a Schottky-type

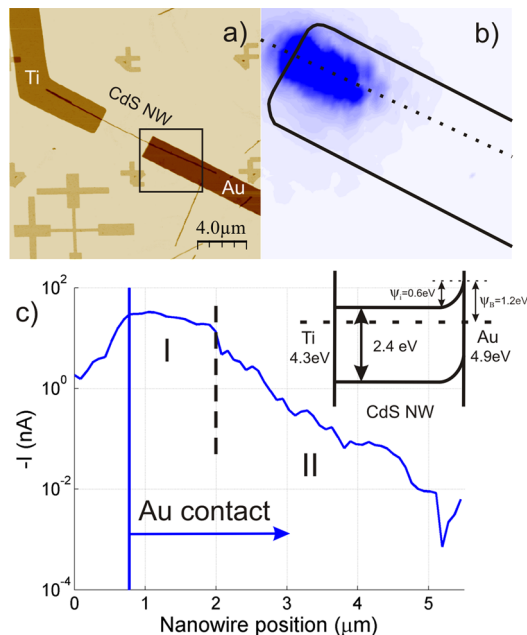


**Figure 1.** (a) AFM image of a CdS NW contacted by a gold and titanium electrode. (b) Photocurrent map of the area marked by the black rectangle in panel (a). (c) Photocurrent profile along the dotted line in panel (b). The inset depicts the energy band diagram in the dark of the NW with a titanium and gold contact under short circuit condition. The numbers indicate the respective work functions of the two metals.

contact on the wires resulted in a pronounced photoresponse around the edge of the gold contact, as exemplified by the photocurrent map in Figure 1b. Similar behavior has been reported for different other NWs.<sup>12,19</sup> While previous works have focused on the signal along the bare NW section, we address in the present study the photoresponse along the Schottky contact between the gold layer and the underlying wire segment. Like for the bare wire section, this response originates from the separation of photoexcited electron–hole pairs in the CdS NW by the electric field of the Schottky contact. While the holes are transferred into the gold electrode, the internal field drives the electrons along the NW to the titanium contact. In the corresponding photocurrent profile in Figure 1c (taken along the dotted line in Figure 1b) two different regimes can be distinguished, specifically region I wherein the current remains almost constant over approximately 1  $\mu\text{m}$  from the electrode edge, and region II displaying an exponential current decrease, detectable up to 5  $\mu\text{m}$  into the contact region.

To further analyze the photocurrent profiles, we performed two-dimensional finite element (FEM) calculations based on the open-source package PoissonNL (see Supporting Information for further details) to solve the following set of differential equations, which are based upon the Poisson and the continuity equations for electrons and holes:

$$\vec{\nabla} \cdot (\epsilon_r \vec{\nabla} V) = -\rho / \epsilon_0$$

$$\vec{\nabla} \cdot (\mu_e n \vec{\nabla} \psi_e) = 0$$

$$\vec{\nabla} \cdot (\mu_h p \vec{\nabla} \psi_p) = 0$$

where  $\rho$  is the charge density,  $\epsilon_r$  the relative dielectric constant,  $\epsilon_0$  the vacuum permittivity,  $\mu_{e(h)}$  the electron (hole) mobility,  $n(p)$  the electron (hole) density,  $V$  the electric potential, and  $\psi_{n(p)}$  the quasi-Fermi level for electrons (holes). The material constants used for the calculation are summarized in Table 1.

**Table 1. Material Constants of Cadmium Sulfide**

bandgap	2.482 eV <sup>22</sup>	electron mobility	$300 \text{ cm}^2/(\text{V s})^{11,25}$
effective density of states	$2.4 \text{ e}^{18} \text{ cm}^{-3}^{23}$	hole mobility	$50 \text{ cm}^2/(\text{V s})^{11,25}$
electron affinity	3.7 eV <sup>24</sup>	dielectric constant	8.73 <sup>20</sup>

Figure 2a shows a schematic drawing of the simulated mesh representing the CdS/Au contact. In Figure 2b, the calculated electric potential map is depicted for the device under short circuit condition. The titanium electrode is defined as source at 0 V. From the work function difference between the gold electrode and the CdS, one obtains a Schottky barrier height of  $\psi_B = 1.2 \text{ eV}$  (see Figure 1c),<sup>17</sup> which leads to a contact potential<sup>21</sup> of  $\psi_i = 0.6 \text{ V}$ . The electric field distribution calculated using the relation  $\vec{E} = -\vec{\nabla}V$  in the  $x$ - and  $y$ -direction within the CdS NW is illustrated by Figure 2c,d, respectively. The white arrows in the color maps indicate the direction of the electric field-induced forces on electrons, according to the relation  $\vec{F} = -q\vec{E}$  with the positive elementary charge  $q$ .

The maximum of the  $E_x$  component ( $\sim 1 \text{ MV/m}$ ) is located just outside of the metal contact (Figure 2e). Excited electrons in the NW are moved by the  $E_x$  field in axial direction toward the titanium contact. As the electrical field also extends below the electrode, electrons at this location are pushed out of the contact. The exponential decay of the  $E_x$  component below the electrode is largely independent of any applied bias. Even if bias is applied, the potential along the gold electrode remains constant and with it the axial electric field distribution (see Figure S1, Supporting Information). The  $E_y$  component, which assumes a similarly strong magnitude ( $\sim 1 \text{ MV/m}$ ), exerts a force on the electrons toward the CdS/SiO<sub>2</sub> interface. In the following, the radial and axial electric fields will be utilized to simulate the photoresponse below the gold contact and thereby to determine the electron recombination rates.

Modeling the photocurrent along the NW requires solving the continuity equation under illumination. Although the illumination intensity is high ( $\sim 190 \text{ kW/cm}^2$ ), only a small fraction is absorbed by the NW due to appreciable light absorption and scattering by the top gold layer. Finite-difference time-domain (FDTD) calculations of the sample structure based on the MEEP software package<sup>22</sup> yield an absorption coefficient of only  $\alpha = 10^{-4}$  for the CdS NW. Based

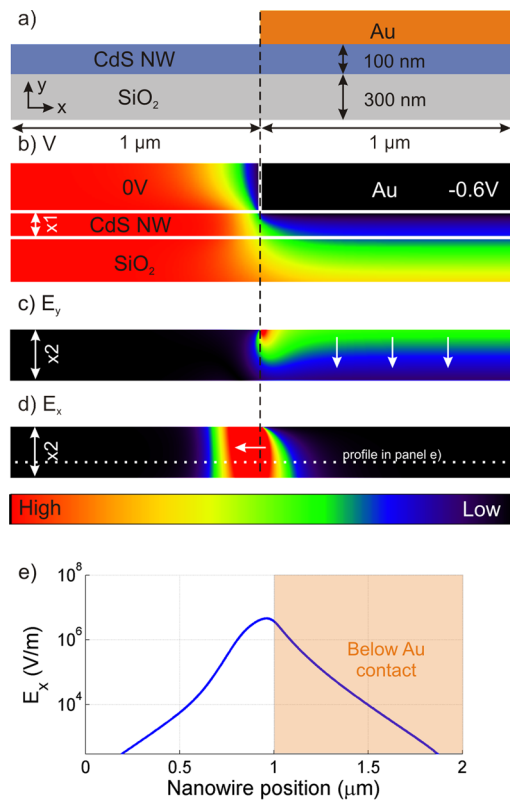


**Figure 2.** Result of a two-dimensional FEM calculation of the potential map at the Au/CdS NW contact. (a) Schematic representation of the simulation space with the relevant dimensions. (b) Calculated electric potential distribution plotted as a color map. (c,d) The calculated y- and x-component of the electric field, respectively. For clearer graphical representation, the maps were vertically stretched. The white arrows indicate the force direction acting on electrons in the NW. (e) Semilogarithmic plot of the  $E_x$  component along the bare and gold-coated wire sections, corresponding to a profile taken along the dotted line in (d).

on the total absorbed power, the maximum induced charge carrier concentration is estimated to be  $3 \times 10^{15} \text{ cm}^{-3}$  (see Supporting Information). This value is sufficiently below the NW doping level of  $10^{16} \text{ cm}^{-3}$ , such that the device remains in the low injection regime where the holes can be treated as minority carriers. Furthermore the diffusion lengths of electrons and holes ( $L \sim 0.7\text{--}1.5 \mu\text{m}$ )<sup>11</sup> are much larger than the NW diameter ( $<100 \text{ nm}$ ), leading to a nearly uniform radial charge distribution in the wire. Therefore, the charge transport can be effectively treated as a one-dimensional problem. Moreover, the holes can be neglected, as they represent only minority carriers.

To describe the transport, the time-independent continuity equation has to be solved:

$$\frac{dn_e(x)}{dt} = G_e - R_e - \operatorname{div} j_e = 0 \quad (1)$$

where  $n_e(x)$  is the electron excess charge, and  $j_e$  is the electron current density, while  $G_e$  and  $R_e$  are the electron generation and recombination rate, respectively. Their difference gives the position-dependent recombination rate of excess electrons:

$$G_e - R_e = -\frac{n_e(x)}{\tau} \quad (2)$$

where  $\tau$  is the electron lifetime. On this basis, the current density  $j_e$  is obtained as the sum of the diffusion and drift currents:

$$j_e = -D_e \frac{dn_e(x)}{dx} + n_e(x) \mu_e E(x) \quad (3)$$

where  $D_e$  is the diffusion coefficient (given by the Einstein relation  $D_e = \mu_e kT/q$ ). To solve eq 1, the electric field, the electron lifetime, and the boundary conditions have to be specified (see Figure 3). For the electric field, the distribution

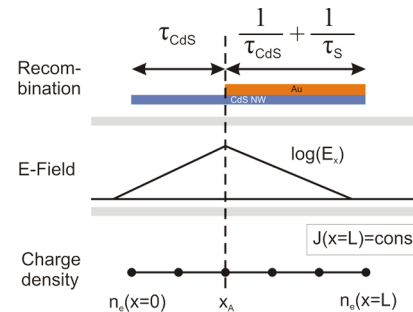


**Figure 3.** Schematic representation of the boundary conditions and the E-field distribution as well as the recombination rates used for solving the drift and diffusion equation in one dimension.

gained by the FEM calculation (Figure 2e) is used. In addition, the Poisson equation is solved to account for Coulomb repulsion along the NW. The resulting electric fields of  $\sim 10^4 \text{ V/m}$  are expected to have only little influence on the transport along the NW. The position of maximal electric field is denoted by  $x_A$  corresponding to the edge of gold contact.

It should be noted that thermoelectric effects are not taken into account in this calculation, as in general they have only a minor influence on the charge transport in semiconductor NWs.<sup>19</sup> Additionally, the top gold electrode acts as an effective temperature sink, preventing the formation of a sizable temperature gradient. The recombination rate ( $1/\tau$ ) along the bare wire is determined by the electron lifetime  $\tau = \tau_{\text{CdS}}$  of pristine CdS,<sup>11</sup> whereas in the gold-coated segment the electron lifetime will be reduced according to

$$\frac{1}{\tau} = \frac{1}{\tau_{\text{CdS}}} + \frac{1}{\tau_s} \quad (4)$$

where  $\tau_s$  accounts for an increased recombination of electrons with the near metal interface of the gold contact.

By choosing an appropriate boundary condition at the right border of the simulation space (Figure 3,  $x = L$ ), the injection of excess electrons (via laser illumination) is implemented (see below for more details).

Solving the differential eq 1 within the above framework yields the charge distribution along the NW, as shown in Figure 4a. It can be seen that at the charge injection point ( $x = L$ ), the electron density  $n_e(x)$  reaches its maximum. Upon approaching the electrode edge,  $n_e(x)$  steeply decreases (region  $\alpha$ ) due to recombination. At the electrode edge (position  $\beta$ ), the electric field becomes so strong that the drift component of  $j_e$  (see eqs 1 and 3) extracts charge carriers from below the contact, leading to charge accumulation outside the contact (region  $\gamma$ ). This effect explains the minimum in the charge carrier density at the electrode edge. Further away from the contact (region  $\delta$ ) the charge carrier density decreases more slowly, due to the

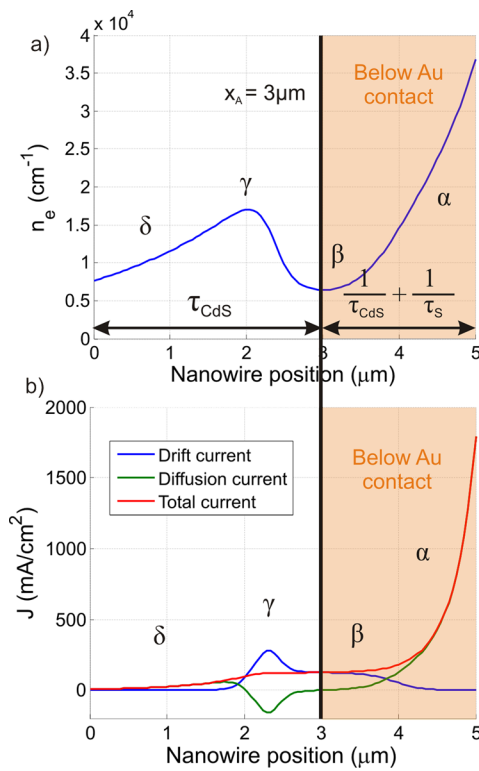


**Figure 4.** Calculated charge carrier density (a) and current density (b) along the CdS NW.

longer electron lifetime  $\tau_{\text{Cds}}$ . Based upon the charge distribution  $n_e(x)$ , the current along the NW can be calculated with the aid of eq 3. Thus obtained components of drift and diffusion currents are plotted in Figure 4b. Within region  $\alpha$ , away from the electrode edge, the current is mainly driven by diffusion. As expected for such type of transport, it exhibits an exponential decrease as a consequence of recombination. Within region  $\beta$  the drift current becomes dominant (compare with  $E_x$  in Figure 2e), while the diffusion current vanishes due to the local minimum in  $n_e(x)$ . This crossover of transport characteristics leads to the shape of the current profile in Figure 1c.

In order to simulate entire photocurrent profiles, the continuity equation has to be solved for the corresponding range of charge injection (illumination) points (as illustrated by Figure S2, Supporting Information). Figure 5a presents a calculated current profile (blue curve) and the measured data points from Figure 1c (green crosses), which are well reproduced by the model. While the exponential decay in region II can be attributed to the diffusion-limited current with its strong recombination characteristic, the constant current in region I arises from the high-electric field close to the electrode edge which efficiently extracts all charges out of the contact. To properly account for this effect, it is necessary to choose the appropriate boundary condition. This precludes fixing the carrier density  $n_e(x = L)$  to a constant value, corresponding to an infinite reservoir of charge carriers, as in this scenario, there would be no electric field which could deplete this reservoir, and the current profile would simply show an exponential decay. Instead, it needs to be considered that due to the spatially limited illumination, only a finite amount of charge carriers can be excited, and accordingly it is the current density which has to be set constant (see Figure 3).

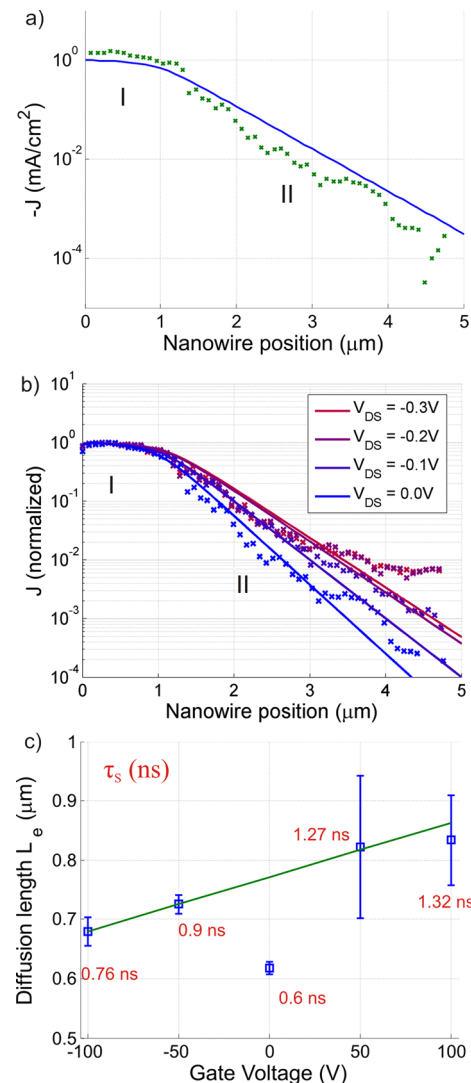


**Figure 5.** (a) Calculated photocurrent profile (blue curve) along the gold-coated CdS NW section and measured data points (green crosses) from Figure 1c. (b) Measured and calculated photocurrent profiles along the same wire section for different applied bias voltages. (c) Electron diffusion length (error bars from the fitting of the experimental data) plotted as a function of the applied gate voltage. The red numbers are the corresponding lifetimes  $\tau_s$  at each data point.

We have furthermore measured the influence of the source-drain bias on the photocurrent profiles. The normalized experimental curves in Figure 5b display a noticeable change in the slope, an observation that cannot be rationalized by the axial component of the electric field ( $E_x$ ) which penetrates maximally  $1\mu\text{m}$  into the contact (see Figure S1, Supporting Information). A plausible alternative explanation involves an increase in the radial  $E_y$  component which is expected to confine the electrons even closer to the  $\text{SiO}_2$  interface and thus reduce the recombination rate. The 2D FEM calculations reveal that the reason why the  $E_y$  component is at all affected by the bias is the presence of the backgate which fixes the potential at some distance to zero. This conclusion gains support from the experimental finding that a similar effect occurs upon the application of a gate voltage. In Figure 5c, the measured variation of the electron diffusion length  $L_e$ , calculated from  $L_e = (D_e \cdot \tau)^{1/2}$ , is plotted against the applied backgate voltage. Following the method of Gu et al.,<sup>11</sup> the product  $\mu_e \tau_{\text{Cds}}$  can be

determined for the CdS NWs. By assuming an electron mobility of  $\mu_e = 300 \text{ cm}^2/(\text{V s})^{11,25}$  and using eq 4, the recombination rate  $1/\tau$  is obtained, which is included in the plot of Figure 5c. It should be mentioned that besides the change in the  $E_y$  component, an additional mechanism might play a role. This becomes evident from the intrinsic electron lifetime of CdS  $\tau_{\text{CdS}}$  given by the relation:

$$\tau_{\text{CdS}} = \frac{1}{R_{\text{ec}} \cdot N_A}$$

where  $R_{\text{ec}}$  is a material parameter depending on the recombination rate, and  $N_A$  is the hole concentration. Correspondingly, by increasing the hole concentration due to the gating, electron–hole pair recombination becomes more probable, which is expected to lower the electron lifetime.

In summary, we have used the spatially resolved photoresponse of the Schottky-type contact between gold and a CdS NW to determine the electron recombination behavior of the wires. This was achieved by solving the corresponding drift and diffusion equations, and further simulations helped understanding the mechanisms behind the bias- and gate voltage-induced changes of the measured photocurrent profiles. Our results reveal an efficient charge carrier extraction region in nanoscale Schottky contacts. The situation is different for thick semiconductor layers in bulk devices, in which case the charge carriers would penetrate much further into the CdS. This results in a fast decrease of the horizontal electric field with increasing distance from the electrode, preventing easy charge extraction in such a configuration.

## ■ ASSOCIATED CONTENT

### Supporting Information

Additional information and graphs concerning the numerical calculations on the drift and diffusion equation. This material is available free of charge via the Internet at <http://pubs.acs.org>.

## ■ AUTHOR INFORMATION

### Corresponding Author

\*E-mail: t.dufaux@fkf.mpg.de

### Notes

The authors declare no competing financial interest.

## ■ ACKNOWLEDGMENTS

This work was supported by the Bundesministerium für Bildung und Forschung (BMBF) within the framework of the SONAPOLY project. The authors thank D. Kälblein for valuable discussions.

## ■ REFERENCES

- (1) Tian, B.; Zheng, X.; Kempa, T.; Fang, Y.; Yu, N.; Yu, G.; Huang, J.; Lieber, C. M. *Nature* **2007**, *449*, 885.
- (2) Hayden, O.; Agarwal, R.; Lieber, C. M. *Nat. Mater.* **2006**, *5*, 352.
- (3) Jie, J. S.; Zhang, W. J.; Jiang, Y.; Meng, X. M.; Li, Y. Q.; Lee, S. T. *Nano Lett.* **2006**, *6* (9), 1887.
- (4) Soci, C.; Zhang, A.; Xiang, B.; Dayeh, S. A.; Aplin, D. P. R.; Park, J.; Bao, X. Y.; Lo, Y. H.; Wang, D. *Nano Lett.* **2007**, *7* (4), 1003.
- (5) Chen, R. S.; Chen, H. Y.; Lu, C. Y.; Chen, K. H.; Chen, C. P.; Chen, L. C.; Yang, Y. *J. Appl. Phys. Lett.* **2007**, *91*, 223106.
- (6) Zhu, J.; Yu, Z.; Burkhard, G. F.; Hsu, C.-M.; Connor, S. T.; Xu, Y.; Wang, Q.; McGehee, M.; Fan, S.; Cui, Y. *Nano Lett.* **2009**, *9* (1), 279.
- (7) Fan, Z.; Razavi, H.; Do, J.-W.; Moriwaki, A.; Ergen, O.; Chueh, Y.-L.; Leu, P. W.; Ho, J. C.; Takahashi, T.; Reichertz, L. A.; Neale, S.; Yu, K.; Wu, M.; Ager, J. W.; Javey, A. *Nat. Mater.* **2009**, *8*, 648.
- (8) Dufaux, T.; Boettcher, J.; Burghard, M.; Kern, K. *Small* **2010**, *6*, 1868.
- (9) Soci, C.; Zhang, A.; Bao, X. Y.; Kim, H.; Lo, Y.; Wang, D. J. *Nanosci. Nanotechnol.* **2010**, *10*, 1.
- (10) Balasubramanian, K.; Burghard, M.; Kern, K.; Scolari, M.; Mews, A. *Nano Lett.* **2005**, *5*, 507–510.
- (11) Gu, Y.; Romankiewicz, J. P.; David, J. K.; Lensch, J. L.; Lauhon, L. J. *Nano Lett.* **2006**, *6* (5), 948.
- (12) Kelzenberg, M. D.; Tuner-Evans, D. B.; Kayes, B. M.; Filler, M. A.; Putnam, M. C.; Lewis, N. S.; Atwater, H. A. *Nano Lett.* **2008**, *8* (2), 710.
- (13) Lee, E. J. H.; Balasubramanian, K.; Dorfmüller, J.; Vogelgesang, R.; Fu, N.; Mews, A.; Burghard, M.; Kern, K. *Small* **2007**, *3* (12), 2038.
- (14) Lee, E. J. H.; Balasubramanian, K.; Weitz, R. T.; Burghard, M.; Kern, K. *Nat. Nanotechnol.* **2008**, *3*, 486.
- (15) Dufaux, T.; Dorfmüller, J.; Vogelgesang, R.; Burghard, M.; Kern, K. *App. Phys. Lett.* **2010**, *97*, 161110.
- (16) Panayotatos, P.; Card, H. C. *Sol. Stat. Electronics* **1979**, *23*, 41.
- (17) Oktik, S.; Russell, G. J.; Woods, J. *Semicond. Sci. Technol.* **1987**, *2*, 661.
- (18) Gu, Y.; Romankiewicz, J. P.; David, J. K.; Lensch, J. L.; Lauhon, L. J.; Kwak, E.-S.; Kwak, T. W.; Odom, T. W. *J. Vac. Sci. Technol., B* **2006**, *24*, 2172.
- (19) Fu, D.; Zou, J.; Wang, K.; Zhang, R.; Yu, D.; Wu, J. *Nano Lett.* **2011**, *11* (9), 3809.
- (20) Sze, S. M.; Ng, K. K. *Physics of Semiconductor Devices*; John Wiley & Sons: Hoboken, NJ, 2006.
- (21) Oskooi, A. F.; Roundy, D.; Ibanescu, M.; Bermel, P.; Joannopoulos, J. D.; Johnson, S. G. *Comput. Phys. Commun.* **2010**, *181*, 687.
- (22) Madelung, O. *Semiconductors: Data Handbook*; Springer-Verlag: Berlin, Germany, 2004.
- (23) Frank, A. J.; Glenis, S.; Nelson, A. J. *J. Phys. Chem.* **1989**, *93* (9), 3818.
- (24) Van de Walle, C. G.; Neugebauer, J. *Nature* **2003**, *423*, 626.
- (25) Ma, R.-M.; Dai, L.; Qin, G.-G. *Nano Lett.* **2007**, *7* (4), 868.